

See discussions, stats, and author profiles for this publication at: <https://www.researchgate.net/publication/251629612>

Precision flight control for a multi-vehicle quadrotor helicopter testbed. Control Engineering Practice, 19(9), 1023-1036

Article in Control Engineering Practice · September 2011

Impact Factor: 1.81 · DOI: 10.1016/j.conengprac.2011.04.005

CITATIONS

78

READS

205

4 authors, including:



[Gabriel Hoffmann](#)

Zee.Aero

28 PUBLICATIONS 2,405 CITATIONS

SEE PROFILE



[Steven L. Waslander](#)

University of Waterloo

88 PUBLICATIONS 1,178 CITATIONS

SEE PROFILE

Precision Flight Control for A Multi-Vehicle Quadrotor Helicopter Testbed

Gabriel M. Hoffmann^{a,1}, Haomiao Huang^{a,1}, Steven L. Waslander^{b,1}, Claire J. Tomlin^c

^a *Aeronautics & Astronautics
Stanford University
Stanford, CA 94305*

gabe.hoffmann@gmail.com, haomiao@stanford.edu

^b *Department of Mechanical and Mechatronics Engineering
University of Waterloo
Waterloo, ON, Canada, N2L 3G1
stevenw@uwaterloo.ca*

^c *Electrical Engineering and Computer Sciences
University of California Berkeley
Berkeley, CA 94708
tomlin@eecs.berkeley.edu*

Abstract

Quadrotor helicopters continue to grow in popularity for unmanned aerial vehicle applications. However, accurate dynamic models for deriving controllers for moderate to high speeds have been lacking. This work presents theoretical models of quadrotor aerodynamics with non-zero free-stream velocities based on helicopter momentum and blade element theory, valianced with static tests and flight data. Controllers are derived using these models and implemented on the Stanford Testbed of Autonomous Rotorcraft for Multi-Agent Control (STARMAC), demonstrating significant improvements over existing methods. The design of the STARMAC platform is described, and flight results are presented demonstrating improved accuracy over commercially available quadrotors.

Keywords: quadrotor helicopters, unmanned aerial vehicles, flight control, quadrotor aerodynamics

1. Introduction

Quadrotor helicopters are an increasingly popular rotorcraft concept for unmanned aerial vehicle (UAV) platforms. These vehicles use two pairs of counter-rotating, fixed-pitch rotors located at the four corners of the aircraft, as shown in Figure 1. Their use as autonomous platforms has been envisaged in a variety of applications, both as individual vehicles and in multiple vehicle teams, including surveillance, search and rescue, and mobile sensor networks [1].

Recent interest in the quadrotor design from numerous communities, including research, surveillance, construction and police use [2], can be linked to two main advantages over comparable vertical take off and landing (VTOL) UAVs, such as helicopters. First, quadrotors can use fixed pitch rotors and direct control of motor speeds for vehicle control, simplifying design and maintenance by eliminating complex mechanical control linkages for rotor actuation. Second, the use of four rotors ensures that individual rotors are smaller than the equivalent main rotor on a helicopter for a given airframe size. The smaller rotors store less kinetic energy during flight and can be enclosed within a protective frame, permitting flights indoors and in obstacle-dense environments with reduced risk of damage to the vehicles, their operators, or surroundings. These added safety benefits greatly accelerate the design and test flight process by allowing testing to take place indoors or out, by inexperienced pilots, and with a short turnaround time for recovery from incidents.

As a result of these advantages, there have been a number of commercial [3, 4, 5, 6] and research [7, 8, 9, 10] quadrotor platforms developed. However, there has been relatively little development of accurate dynamics models of quadrotors for operating at higher speeds and in outdoor environments. Such models and control techniques based

¹These authors contributed equally to this work.

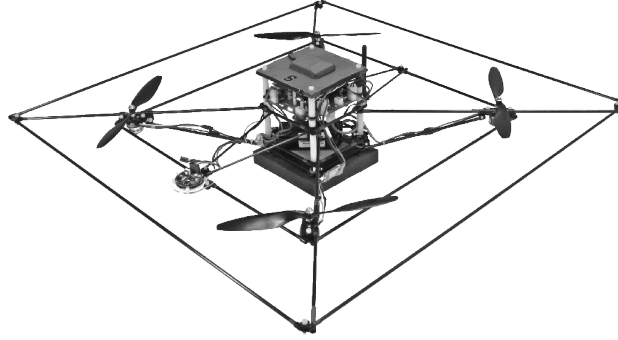


Figure 1: STARMAC II quadrotor helicopter.

upon the models are critical for precision control and trajectory tracking. The main contributions of this work are the presentation of aerodynamic models for quadrotors and the use of these models in the development of a quadrotor platform (the Stanford Testbed of Autonomous Rotorcraft for Multi-Agent Control, or STARMAC) capable of achieving the sub-meter positioning precision necessary to fly multiple vehicles in a confined area with substantial motion.

STARMAC has been developed to take advantage of the benefits of quadrotors, with the aim of being an easy-to-use and reconfigurable proving ground for novel algorithms for multi-agent applications. It is currently comprised of six STARMAC II quadrotors. These vehicles have been used to demonstrate a variety of algorithms, including experiments for collision avoidance [11, 12], information-theoretic control for cooperative search [13, 14], dynamically feasible trajectory generation[15, 16], and verification of provably safe aerobatic maneuvers[17]. In each case, the flexibility and convenience of the quadrotor design in general and the precision flight capabilities of STARMAC in particular have enabled rapid evaluation of new technologies.

In this work, aerodynamic models of quadrotor helicopters are developed, based on well established research for helicopter aerodynamics [18, 19, 20], including the effects of angle of attack and speed on total thrust, and the effect of blade flapping on the direction of thrust and moments acting on the vehicle. The models are valianced with static thrust test stand measurements and incorporated into a nonlinear simulation to compare with flight test results. Second, the models are used to derive nonlinear control laws to counteract the effects of a non-zero free-stream velocity on the quadrotor vehicle in flight. Variations in thrust due to angle of attack and speed are eliminated through feedforward thrust variation, while blade flapping moments are countered through feedforward differential thrust commands. Finally, a comprehensive set of controller designs are proposed for closed loop attitude, altitude, position and trajectory tracking that enable precise execution of the desired path, and are demonstrated in both indoor and outdoor flight test results. Given precise state estimation and aerodynamic modeling, simple control laws produce the desired control precision. Although the models and controls are developed and tested on the STARMAC platform, the results are applicable to the design and control of any general quadrotor helicopter.

The paper proceeds as follows. Section 2 presents a summary of the history of quadrotors and a review of related work. Then, in Section 3 a nonlinear dynamic model of the quadrotor helicopter is developed, with focus on the effects of vehicle motion on the forces and moments produced by the vehicle. The design choices made for STARMAC II are presented in Section 4, including propulsion, frame, sensors, communications, and computational payloads. Finally, the control system design is described in Section 5, with flight test results for each control loop culminating in multiple waypoint trajectory tracking demonstrations with sub-meter accuracy.

2. Related Work

Quadrotor helicopters are controlled by varying the thrust of two sets of counter-rotating rotor pairs, as depicted in Figure 2. Pitch and roll angles are controlled using moments generated by differential thrust between rotors on opposite sides of the vehicle, and the yaw angle is controlled using the difference in reaction torques between the pitch and roll rotor pairs. Vertical position is controlled with the total thrust of all rotors, and lateral acceleration is controlled through the pitch and roll of the aircraft.

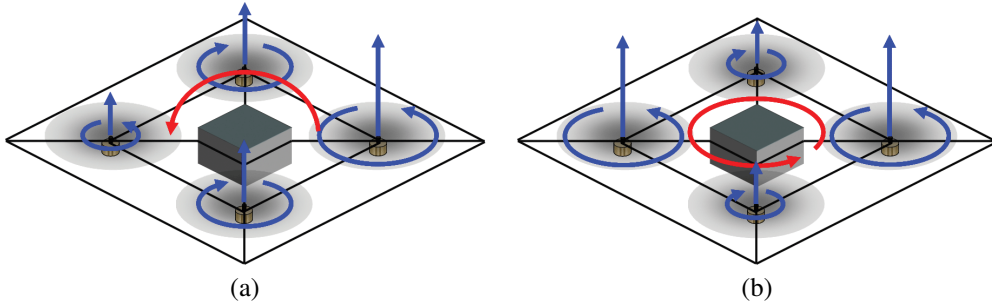


Figure 2: Quadrotor helicopters are controlled by varying thrust at each rotor to produce (a) roll or pitch axis torques, and (b) yaw axis torque.

The first flight-capable quadrotor designs appeared as early as the 1920's [19], though no practical versions were built until more recent advances in microprocessor capabilities and in micro-electro-mechanical system (MEMS) inertial sensors have allowed for automatic stability augmentation systems. These advances have spawned a series of new quadrotor designs, from simple remote control (RC) quadrotor toys such as the Roswell flyer (HMX-4) [21], and Draganflyer [22] to more advanced autonomous aerial vehicles capable of waypoint trajectories and autonomous aerial surveillance tasks.

Increased interest in small quadrotors led to the development of numerous commercially available platforms with autonomous flight capabilities. The MD4-200 quadcopter from Microdrones GmbH [3], available in 2006, Draganfly X4 [5] and Aeryon Scout [6], both available in 2009, are capable of GPS waypoint tracking. The Hummingbird and Pelican from Ascending Technologies are similarly capable. The estimation and control for these vehicles use single-frequency GPS, with accuracy of 5 m circular error precision (CEP), resulting in position control errors of similar magnitude (demonstrated 5-10 m error depending on wind conditions for the Aeryon Scout and 3-5m for the Pelican, estimated for other platforms). These systems are intended for open spaces, low speed operations, and moderate wind conditions.

For autonomous operation in cluttered environments through accurate trajectory control, work on the OS4 quadrotor [23] identified several dynamic effects beyond the rigid body equations of motion, including gyroscopic torque, angular acceleration of blades, drag force on the vehicle, and rotor blade flapping. Back-stepping control was used to improve on the vehicle's initial linear control law and reduce position control errors. Similarly, the X-4 project at the Australian National University [24] considered the effects of blade flapping, roll and pitch damping due to differing relative ascent rates of opposite rotors, and rotor design, and showed preliminary results considering these effects for vehicle and rotor design in flight tests [25, 26].

Recent research in quadrotor design focuses on extending these capabilities for more complex missions [27, 21, 23, 28, 29, 30, 31, 25, 32, 8, 9, 10, 33] with more demanding system requirements. The range of projects resulted in vehicles from 0.3 to 4.0 kg, and demonstrate a variety of designs and control techniques that seek to extend vehicle capabilities to more complex tasks. Specifically, the STARMAC platform [27] was developed with the dual aims of enabling autonomous operation in constrained environments as well as allowing multiple vehicles to operate in close proximity for team missions that benefit from multiple simultaneous viewpoints. The combination of these two capabilities opens the door to many new applications.

One important emerging application area is the focus on convenient indoor quadrotor testbeds, with similarly stringent positioning requirements for safe operation in close proximity to obstacles in the environment, though mostly operating at low speeds. The SWARM project [7] focuses on multi-vehicle coordination and demonstrated impressive multi-vehicle trajectory tracking control using Draganflyer V Ti Pro quadrotors with LQR control. Sensing and computation occur off-board on a centralized platform using the Vicon positioning system indoors at low speeds. More recent efforts have developed a vehicle capable of autonomous indoor exploration using a laser scanner and stereo vision [8], which performs computation off board as well. The GRASP lab has shown results with a group of quadrotors carrying out coordinated flights for carrying a single load with multiple vehicles [9]. Finally, an indoor flight system has been developed successfully demonstrating certain extreme flight maneuvers in a controlled environment [10]. Both of these last efforts use the Vicon positioning system and off-board state estimation.

The precision flight capability of existing designs intended for outdoor flight, both commercial and academic, are typically insufficient for operation with any significant speed in constrained environments. Also, while many research platforms have demonstrated advanced capabilities in controlled, indoor environments with off-board computation, very few have been developed for self-sufficient autonomous multi-vehicle operation. The work presented in this paper focuses on a novel quadrotor helicopter design that is capable of flying both indoors and outdoors at significant speeds, and can carry sufficient sensing and computing resources not only to localize and control the aircraft, but also to enable higher levels of vehicular autonomy. Some preliminary versions of these results were presented in [34, 35].

3. Vehicle Aerodynamics

A detailed development of the aerodynamics of quadrotor helicopters is now presented. First, the vehicle's full nonlinear dynamics are presented. Then, the vehicle's input forces and moments are computed for non-zero free-stream velocities based on techniques from helicopter analysis. These inputs are used in the development of vehicle controllers in Section 5.

3.1. Inertial Dynamics

The derivation of the nonlinear dynamics is performed in North-East-Down (NED) inertial and body fixed coordinates. Let $\{\mathbf{e}_N, \mathbf{e}_E, \mathbf{e}_D\}$ denote unit vectors along the respective inertial axes, and $\{\mathbf{x}_B, \mathbf{y}_B, \mathbf{z}_B\}$ denote unit vectors along the respective body axes, as shown in Figure 3. Euler angles to rotate from NED axes to body fixed axes are the 3-2-1 sequence $\{\psi, \theta, \phi\}$, referred to as yaw, pitch, and roll, respectively. The current velocity direction unit vector is \mathbf{e}_v , in inertial coordinates. The direction of the projection of \mathbf{e}_v onto the $\mathbf{x}_B - \mathbf{y}_B$ plane defines the direction of \mathbf{e}_{lon} in the body-fixed longitudinal, lateral, vertical frame, $\{\mathbf{e}_{lon}, \mathbf{e}_{lat}, \mathbf{e}_{ver}\}$, as shown in Figure 8. Due to blade flapping, the rotor plane does not necessarily align with the $\mathbf{x}_B, \mathbf{y}_B$ plane, so for the j^{th} rotor let $\{\mathbf{x}_{R_j}, \mathbf{y}_{R_j}, \mathbf{z}_{R_j}\}$ denote unit vectors aligned with the plane of the rotor and oriented with respect to the $\{\mathbf{e}_{lon}, \mathbf{e}_{lat}, \mathbf{e}_{ver}\}$ frame. Let \mathbf{x} be defined as the position vector from the inertial origin to the vehicle c.g., and let ω_B be defined as the angular velocity of the aircraft in the body frame.

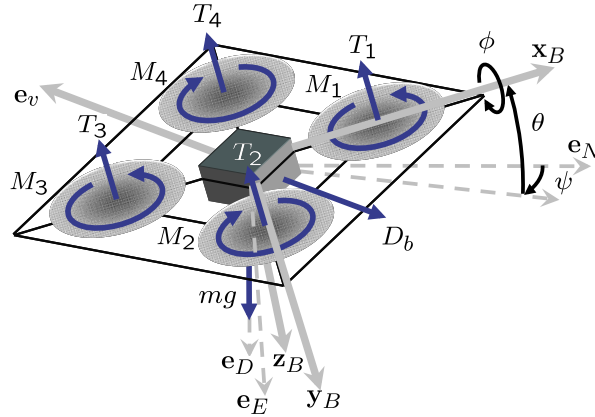


Figure 3: Free body diagram of a quadrotor helicopter.

The rotors, numbered 1 – 4, are mounted outboard on the $\mathbf{x}_B, \mathbf{y}_B, -\mathbf{x}_B$ and $-\mathbf{y}_B$ axes, respectively, with position vectors \mathbf{r}_j with respect to the c.g. The thrust T_j produced by the j^{th} rotor acts perpendicularly to the rotor plane along the \mathbf{z}_{R_j} axis, as defined in Figure 4. The vehicle body drag force is $D_b \propto v_\infty^2$, vehicle mass is m , acceleration due to gravity is g , and the inertia matrix is $I_B \in \mathbb{R}^{3 \times 3}$. A free body diagram is depicted in Figure 3, with a depiction of the rotor forces and moments in Figure 4. The total force, \mathbf{F} , can be summed as,

$$\mathbf{F} = -D_b \mathbf{e}_v + mg \mathbf{e}_D + \sum_{j=1}^4 (-T_j R_{R_j, I} \mathbf{z}_{R_j}) \quad (1)$$

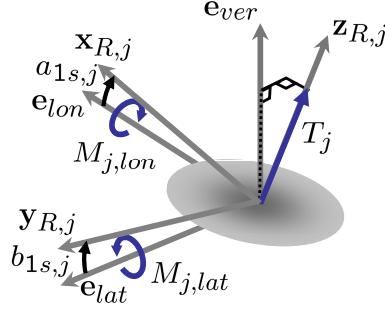


Figure 4: Free body diagram of the moments and forces acting on rotor j .

where $R_{R_j,I}$ is the rotation matrix from the plane of rotor j to inertial coordinates. Similarly, the total moment, \mathbf{M} , is,

$$\mathbf{M} = \sum_{j=1}^4 (\mathbf{M}_j + \mathbf{M}_{bf,j} + \mathbf{r}_j \times (-T_j R_{R_j,B} \mathbf{z}_{R_j})) \quad (2)$$

where $R_{R_j,B}$ is the rotation matrix from the plane of rotor j to body coordinates. Note that the drag force was neglected in computing the moment. This force was found to cause a negligible disturbance on the total moment over the flight regime of interest, relative to blade flapping torques. The full nonlinear dynamics can be described as,

$$\mathbf{F} = m\ddot{\mathbf{x}} \quad (3)$$

$$\mathbf{M} = I_B \dot{\omega}_B + \omega_B \times I_B \omega_B \quad (4)$$

where the total angular momentum of the rotors is assumed to be near zero, as the momentum from the counter-rotating pairs cancels when yaw is held steady.

3.2. Aerodynamic Forces and Moments

Although quadrotor helicopter dynamics are often modeled as independent of free-stream velocity for attitude and altitude control, this assumption is only reasonable at low velocities. Even at moderate velocities, the impact of the aerodynamic effects resulting from variation in air speed is significant.

Two main effects are presented here that have each been experimentally observed on the STARMAC platform. The first effect is the variation in total thrust from a rotor with free-stream velocity and angle of attack, and the second is the effect known as “blade flapping”, resulting from the differing flow velocities experienced by advancing and retreating blades of a rotor in translational flight. Aerodynamic drag, a reaction force proportional to speed squared, will not be discussed because it is both vehicle design-dependent and already well known. At moderate speeds, both experimental results and the literature [19] show that the effect of drag on rotorcraft is less significant than the following more dominant effects.

3.2.1. Total Thrust

Thrust is produced by each rotor through the torque applied the rotor by a motor. The thrust can be analyzed by equating the power produced by the motors to the ideal power required to generate thrust by changing the momentum of a column of air. At hover, the ideal power, P_h , is

$$P_h = T v_h \quad (5)$$

where the induced velocity at hover, v_h , is the change in air speed induced by the rotor blades with respect to the free-stream velocity, v_∞ .

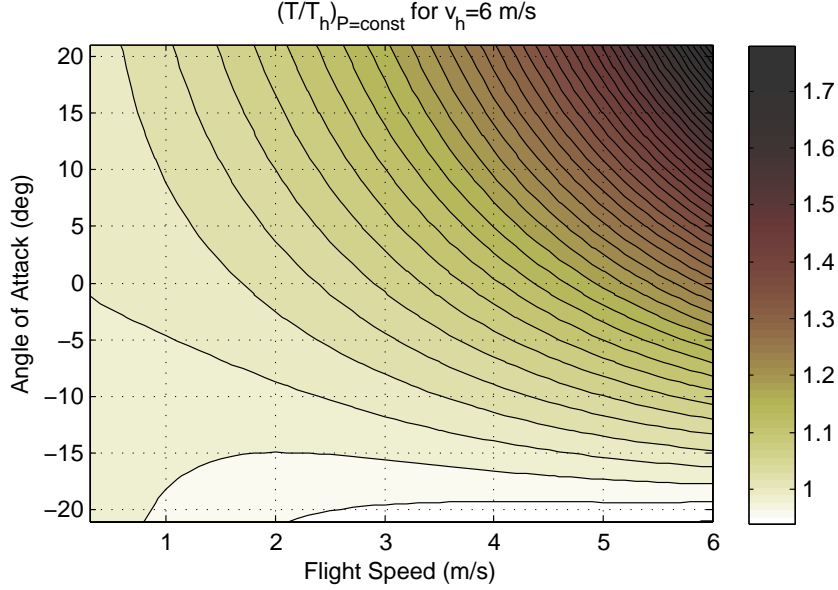


Figure 5: Thrust dependence on angle of attack and vehicle speed.

As a rotorcraft undergoes translational motion or changes its angle of attack, the induced power, the power transferred to the free-stream, changes. To derive the effect of free-stream velocity on induced power from conservation of momentum, the induced velocity v_i of the free-stream by the rotors of an ideal vehicle can be found by solving [19]

$$v_i = \frac{v_h^2}{\sqrt{(v_\infty \cos \alpha)^2 + (v_i - v_\infty \sin \alpha)^2}} \quad (6)$$

for v_i , where α is the angle of attack of the rotor plane with respect to the free-stream, with the convention that positive values correspond to pitching up (as with airfoils). The physical (non-imaginary) solution to this equation is accurate over a wide range of flight conditions as shown by experimental results in the literature [36], especially at small angles of attack. At large angles of attack, the rotor can enter the vortex ring state, at which point the equation no longer holds, as will be described below. Nonetheless, it provides an accurate result for much of the flight envelope, including portions of the flight envelope for which momentum theory is not applicable. Using the expression for v_i , or a numerical solution, the ideal thrust T for power input P can be computed, using

$$T = \frac{P}{v_i - v_\infty \sin \alpha} \quad (7)$$

where the denominator is the air speed across the rotors.

For electric motors, the power applied by each motor varies proportional to the square of the applied voltage [34], thus for a given commanded voltage and related nominal thrust the actual thrust generated varies depending on the translational velocity. The value of the ratio of thrust to hover thrust, T/T_h , is plotted for the v_h of STARMAC II in Figure 6. At low speeds the angle of attack has vanishingly little effect on T/T_h . However, as speed increases T/T_h becomes increasingly sensitive to the angle of attack, varying by a substantial fraction of the aircraft's capabilities. Similar to an airplane, pitching up increases the lift force. The angle of attack for which $T = T_h$ increases with forward speed. For level flight, the power required to retain altitude decreases with the forward speed. However, to maintain speed in level flight, the vehicle must pitch forward more as speed increases to cancel drag, leading to a need for more thrust to maintain altitude. There is an optimum speed for any rotorcraft, greater than zero, at which power to stay aloft is minimized (a reduction from power needs in hover of up to 30% or more) [19]. This speed varies with aircraft configuration.

In the extreme regions of angle of attack close to vertical flight, rotorcraft have three operational modes depending on the vehicle's climb velocity v_c , two of which are solutions to Eq. (6) (where $\cos \alpha = 0$), and one of which is a

recirculation effect that invalidates the assumptions for conservation of momentum [19]. Note that these three modes encompass vertical ascent or descent, and are therefore often encountered. The three modes are defined as follows:

1. Normal working state: $0 \leq \frac{v_c}{v_h}$
2. Vortex ring state (VRS): $-2 \leq \frac{v_c}{v_h} < 0$
3. Windmill brake state: $\frac{v_c}{v_h} < -2$

In normal working state air flows down through the rotor, and in windmill brake state air flows up through the rotor due to rapid descent. In both cases, conservation of momentum can be used to derive the induced velocity. For the normal working state, encompassing hover and ascent conditions, the induced velocity is

$$v_i = -\frac{v_c}{2} + \sqrt{\left(\frac{v_c}{2}\right)^2 + v_h^2} \quad (8)$$

For the windmill braking state, the induced velocity is,

$$v_i = -\frac{v_c}{2} - \sqrt{\left(\frac{v_c}{2}\right)^2 - v_h^2} \quad (9)$$

In the vortex ring state, air recirculates through the blades in a periodic and somewhat random fashion. As a result, the induced velocity varies greatly, particularly over the domain $-1.4 \geq v_c/v_h \geq -0.4$, causing rapid random variation in the thrust [36]. An empirical model [19] of induced velocity in vortex ring state is

$$v_i = v_h \left(\kappa + k_1 \left(\frac{v_c}{v_h} \right) + k_2 \left(\frac{v_c}{v_h} \right)^2 + k_3 \left(\frac{v_c}{v_h} \right)^3 + k_4 \left(\frac{v_c}{v_h} \right)^4 \right) \quad (10)$$

where $k_1 = -1.125$, $k_2 = -1.372$, $k_3 = -1.718$, $k_4 = -0.655$, and κ is the measured induced power factor in hover, with a typical value of around 1.15 [19]. This model compares with the mean of experimental results in the literature, though it fails to capture the periodic nature of vortex entrapment.

To model the dynamics during climb, the power is the thrust times the speed it is applied at, hence

$$T = \frac{P}{v_c + v_i} \quad (11)$$

ignoring profile power (drag) losses. Note that Tv_c is the power consumed by the climbing motion, whereas Tv_i is the induced power transferred into the air. It is typically desirable to avoid the vortex ring state, which can be done by maintaining a substantial forward speed while descending [18].

The thrust achieved for a given input power, ignoring profile power losses, can be computed as a function of climb velocity by substituting Eqs. (8), (9), and (10) into Eq. (11). For typical flight conditions experienced by STARMAC II, the ratio of the thrust to hover thrust at a constant power input is shown in Figure 6, for both the theoretical curve, using the solution to the above equations, and experimental data from a thrust measurement stand using a vertical wind disturbance. As is visible in Figure 6, there is a clear loss of thrust associated with climbing, reducing linearly with climb velocity. Finally, a significant negative climb velocity results in an increase in resulting thrust. In thrust test stand experiments, the loss of thrust with an applied climb velocity was clearly noted. The descent velocity experiments were less conclusive. The descent speeds available with the test apparatus were less than those required for full vortex ring state, though vibration was observed, indicating that unsteady flow did occur.

The effect of angle of attack on the total thrust generated by STARMAC II was consistently observed in flight tests, as shown in Figure 7a, where an earlier generation PID control law is used to control altitude. When the vehicle undergoes a quick roll motion increasing the angle of attack, the thrust increases rapidly, acting as a disturbance on the control system. This reaction is predicted by the equations of motion presented in this section, as shown in a full vehicle simulation in Figure 7b. In Section 5, a control law is presented that is more capable of rejecting these disturbances, with feedback control of total thrust.

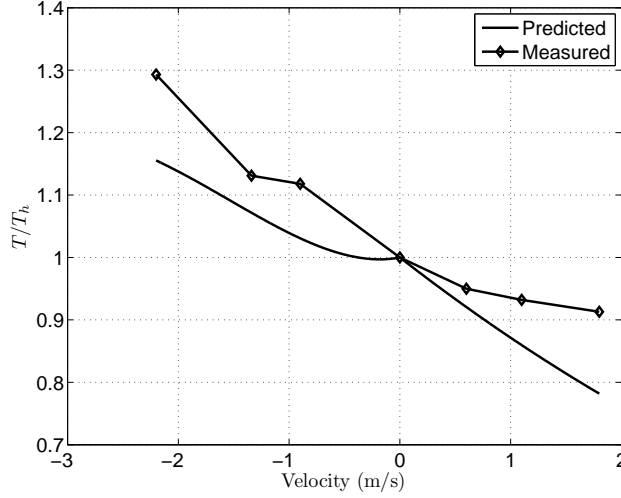


Figure 6: Predicted ideal thrust and measured climb thrust with vertical velocity.

3.2.2. Blade Flapping

The second aerodynamic effect to have a significant impact on the dynamics of quadrotor helicopters is blade flapping. In translational flight, the advancing blade of a rotor has a higher velocity relative to the air, while the retreating blade has a lower velocity, resulting in a variation in lift that causes the rotor blades to flap up and down [20]. This flapping of the blades tilts the rotor plane back from the direction of motion, resulting in a variety of effects on the dynamics of the vehicle, and in particular affecting attitude control performance [25]. For this subsection, the effects on an individual rotor will be considered, so for readability the rotor index, subscript j , is omitted.

The flap angle β of a rotor blade is typically defined in the helicopter literature as the total deflection of a rotor blade away from horizontal in body coordinates at any point in the rotation, and is calculated as

$$\beta = a_{0s} - a_{1s} \cos \Psi + b_{1s} \sin \Psi \quad (12)$$

where a_{0s} is the blade deflection due to coning, a_{1s} and b_{1s} are the longitudinal and lateral blade deflection angles, respectively, due to flapping. The azimuth angle of the blade Ψ is defined to be zero in the direction opposite horizontal velocity of the rotor. The longitudinal deflection gives the amplitude of the rotor tilt when $\Psi = (0, \pi)$ rad, and the lateral deflection is the amplitude when $\Psi = (\pi/2, 3\pi/2)$ rad.

The blade flapping properties of a rotor can differ significantly depending on whether or not the rotor blades are hinged at the base. The equation for deflection angle of a flapping rotor with hinged blades is [25]

$$a_{1s} = \frac{1}{1 + \frac{\mu_{lon}^2}{2}} \frac{4}{3} \left(\frac{C_T}{\sigma} \frac{2}{3} \frac{\mu_{lon} \gamma}{a_0} + \mu_{lon} \right) \quad (13)$$

where a_0 is the slope of the lift curve per radian (typically about 6.0 for conventional airfoils at low Mach numbers [20]). The longitudinal rotor advance ratio, $\mu_{lon} = \frac{v_{lon}}{v_t}$, is the ratio of longitudinal speed to blade tip speed, $v_t = \Omega R$. The nondimensional Lock number, $\gamma = \rho a_0 c R^4 / I_b$, is the ratio of aerodynamic to centrifugal forces, where I_b is the moment of inertia of the blade about the hinge, c is the chord of the blade, and R is the rotor radius. Finally, $\sigma = A_b / A$ is the solidity ratio of the rotor, where A_b is the total area of the rotor blades. The non-dimensionalized torque coefficient is C_T .

The flapping properties of a stiff, fixed-pitch rotor blade, as used on STARMAC II and more typically found on most quadrotors, can be analyzed by modeling the blade as being hinged at an effective offset e_f from the center of rotation (expressed as a percentage of the rotor radius) and a torsional spring with stiffness k_β Nm/rad at the hinge [18]. This approximates the first bending mode of the blade and is sufficient for the small deflection angles of interest. Both e_f and k_β can be determined by measuring the natural frequency ω_n of blade vibration [20, 18]. With these parameters, the equilibrium flapping angles can be determined by solving [18]

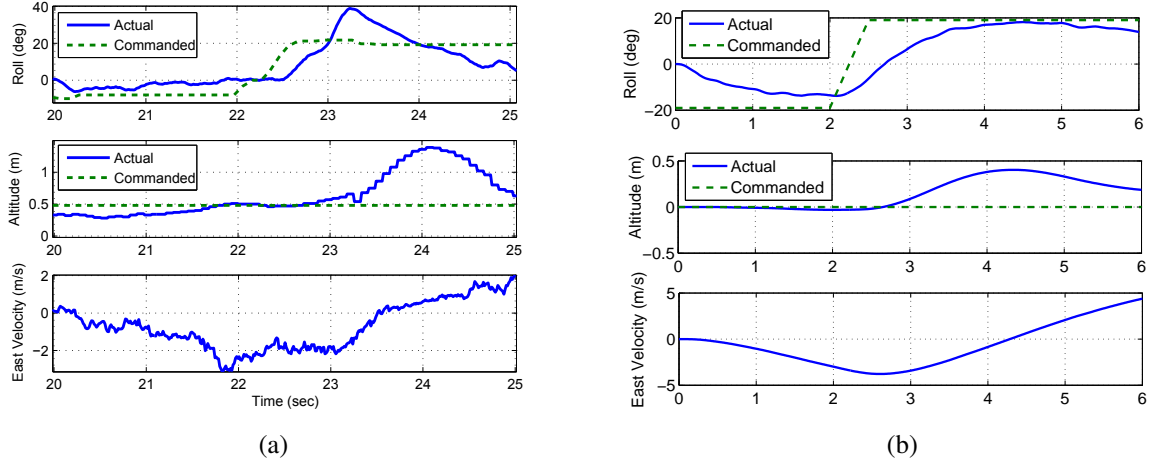


Figure 7: Effect of angle of attack on altitude control, (a) in a flight test using an earlier generation PID controller, and (b) in simulation using the induced power equations.

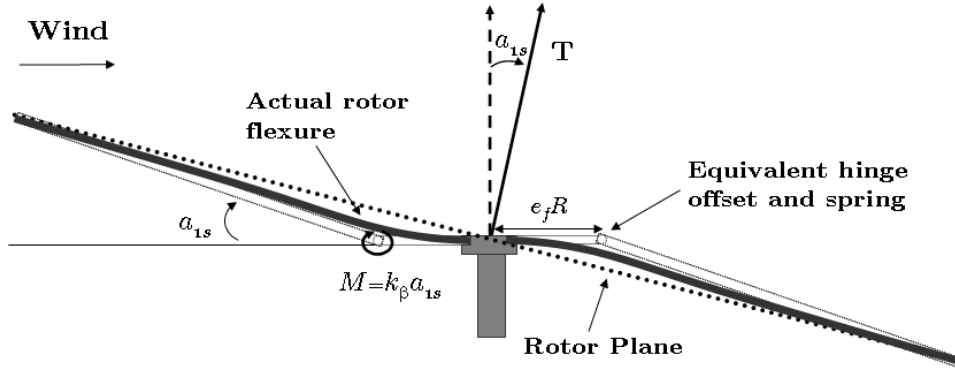


Figure 8: Blade flapping with stiff rotor blades modeled as hinged blades with offset and spring.

$$\begin{bmatrix} \lambda_{\beta}^2 & 0 & 0 & 0 \\ \frac{\gamma}{6}\mu_{lon} & (1 - \lambda_{\beta}^2) & -\frac{\gamma}{8} & 0 \\ 0 & \frac{\gamma}{8} & (1 - \lambda_{\beta}^2) & 0 \\ 0 & 0 & 0 & 1 \end{bmatrix} \begin{bmatrix} a_{0s} \\ a_{1s} \\ b_{1s} \\ \frac{c_T}{\sigma a_0} \end{bmatrix} = \begin{bmatrix} \frac{\gamma}{8} & -\frac{\gamma}{6} \\ 0 & 0 \\ \frac{\gamma}{3}\mu_{lon} & 0 \\ \frac{1}{3} & -\frac{1}{2} \end{bmatrix} \begin{bmatrix} \Theta_{avg} \\ \mu_{ver} + \lambda_i \end{bmatrix} \quad (14)$$

where the induced inflow ratio $\lambda_i = \frac{v_i}{v_t}$. The vertical advance ratio is $\mu_{ver} = \frac{v_{ver}}{v_t}$. The average pitch angle of the blade is Θ_{avg} . λ_{β} is the ratio of the flapping frequency ω_{β} to the angular rate Ω of the rotor, and can be calculated for use in Eq. (14) as

$$\lambda_{\beta} = \sqrt{\left(1 + \frac{3}{2}e_f\right) + \frac{k_{\beta}}{I_b\Omega^2}} \quad (15)$$

Blade flapping causes both longitudinal and lateral thrust forces and moments. For quadrotor helicopters, however, the moments generated by lateral deflections cancel when yaw rates are low relative to airspeed, and generation of unbalanced moments is due entirely to the longitudinal deflection, a_{1s} . The backward tilt of the rotor plane generates longitudinal thrust T_{lon} (see Figure 8),

$$T_{b,lon} = T \sin a_{1s} \quad (16)$$

If the center of gravity (c.g.) is not vertically aligned with the rotor plane, this longitudinal force will generate a

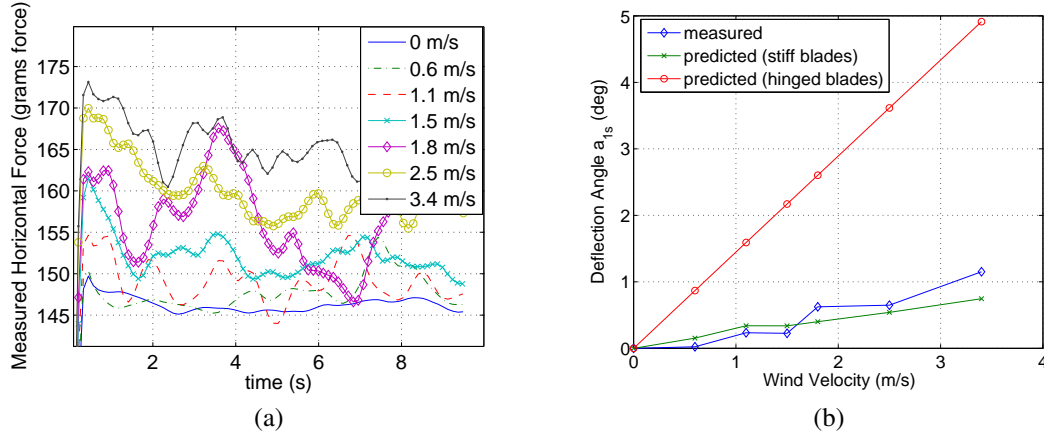


Figure 9: (a) Horizontal force measurements at different wind speeds to calculate the flapping angles. (b) The measured deflection angle compared with predicted values for hinged, freely flapping blades and for stiff, unhinged blades.

moment about the c.g., $M_{b,lon} = T_{b,lon}z_{cg}$, where z_{cg} is the vertical distance from the rotor plane to the c.g. of the vehicle. For stiff rotors, as are used in most current quadrotor helicopters, the tilt of the blades also generates a moment at the rotor hub

$$M_{b,s} = k_{\beta}a_{1s} \quad (17)$$

where k_{β} is the stiffness of the rotor blade in Nm/rad . Finally, $M_{bf} = M_{b,lon} + M_{b,s}$ is the total longitudinal moment created by blade flapping.

To validate the models developed for blade flapping on the STARMAC platform, the thrust test stand was used. The lateral force due to the deflection of the thrust vector by flapping was measured for a single rotor by blowing air at fixed velocities across a spinning rotor attached to the test stand. This data was filtered and used to calculate the average deflection angle as a function of incident wind velocity and compared to the model predictions. Equation (13) predicts a roughly linear relationship between velocity and deflection angle in the shown operating regime. In practice, this equation over-predicts the flapping seen by rotors with non-hinged blades where the stiffness of the blades must be taken into consideration, as in the model presented in Eq. (14). For the flapping equations, ω_n was also measured using the test stand, giving an effective hinge offset of 25% for the Wattage 10×4.5 rotors. The value for k_{β} was measured to be $0.23Nm/rad$.

The results, plotted in Figure 9, clearly indicate that the non-hinged blade flapping model accurately captures the effect of free-stream velocity on the angle of the rotor plane. Note that turbulence caused oscillations in the blade deflection during experiments, so the measurements presented are an average deflection over a period of 20 s.

The effect of blade flapping was consistently observed in flight tests as shown in Figure 10a, where an aircraft controlled by a simple PD control law is disturbed by the moment due to blade flapping, an effect that increases with speed. The equations of motion in this section predict this effect on the control system, as shown in a full simulation of the dynamics in Figure 10b. In Section 5, a control law is presented that is more capable of rejecting these disturbances, actively rejecting discrepancies between desired and actual torques.

The design of the STARMAC quadrotor platform used for model validation and control design is now briefly presented.

4. Design

The first generation vehicle, STARMAC I, was developed from 2003 to 2005 [27, 37]. It was based on the Draganflyer III [22] platform and was envisaged as a lightweight, easy-to-use testbed for multi-vehicle operations. The vehicles were capable of autonomous hover when coupled with off-board state estimation, however limitations in payload, communications, and computation impaired their ability to perform on-board testing of autonomous multi-agent algorithms. As a result of these limitations, STARMAC II was developed to address the following requirements:

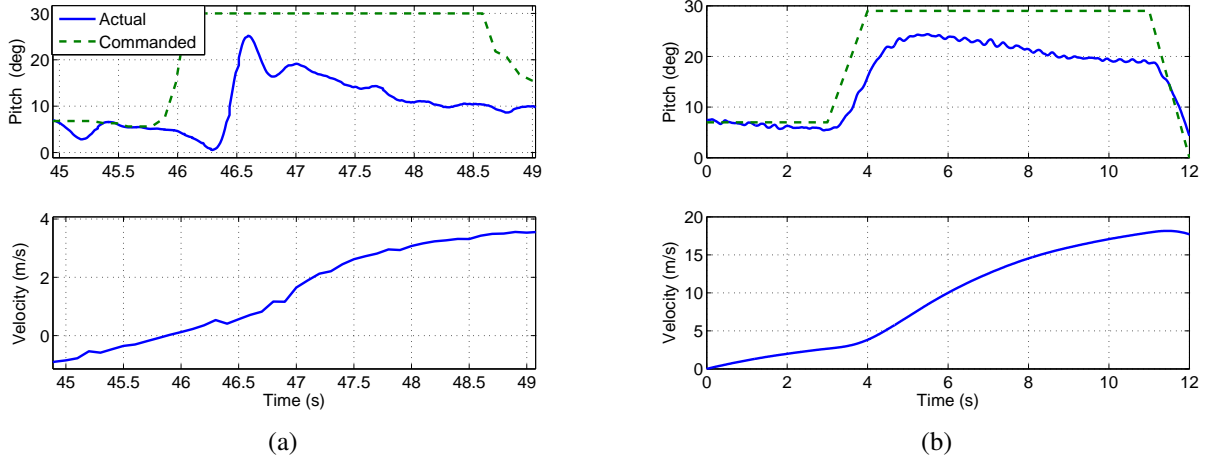


Figure 10: Effect of blade flapping on pitch control, (a) in a flight test using an earlier generation PD controller and (b) in simulation using the blade flapping equations.

1. Safe, simple operation both indoors and outdoors.
2. Onboard autonomous position control and trajectory tracking.
3. Onboard perception of the environment through a variety of sensors.
4. Onboard implementation of multi-vehicle coordination algorithms.

The first requirement drove the selection of the quadrotor helicopter as a safe, easy to use platform with limited maintenance requirements. The ability to hover was deemed essential for operation in confined spaces. The second and third requirements drove the selection of the sensor suite to be included on board the vehicles, that in turn drove the payload requirements. The fourth requirement drove the need for a broadband communication device and the inclusion of significant computational power. There was a tradeoff between keeping the vehicle small enough to easily ensure safety, and making it large enough to support the payload necessary for the applications envisaged for it.

4.1. Vehicle Design

The vehicle frame, shown in Figures 1 and 11, was designed to be as light as possible, while maintaining sufficient stiffness to ensure accurate state measurement and control actuation. The core of the vehicle uses fiberglass laminated honeycomb plates to mount and protect the electronics and provide structural rigidity, and can be vertically expanded to accommodate payloads. The remainder of the frame is carbon fiber tubes and tube straps. This design allows the vehicle to be easily reconfigured for different experiments and payloads. Also, when a collision of sufficient strength occurs, the tubes have some ability to slide in the tube straps rather than breaking, and the tube straps themselves can flex to absorb energy.

The propulsion system was designed for safety and efficiency. The design goal was to maximize flight time and payload capacity, while remaining small and controllable enough to fly in confined indoor environments. The desired payload capacity was a minimum of 0.4 kg for enhanced on-board computation, with 1.0 kg enabling the inclusion of a suite of environment sensors for autonomous operation in unknown surroundings.

The control electronics are comprised of an electronics interface board and several processors. Computation occurs in two stages. The low level processing controls the attitude and altitude dynamics at a fast rate, and the high level processing manages longer computations and position control at a slower rate. The low level computing occurs on an Atmega128 microprocessor that uses measurements from the IMU and ultrasonic rangefinder to control vehicle attitude and altitude at 76 Hz. The high level processing occurs on either a Gumstix Verdex single board computer (SBC) [38] running embedded Linux on a PXA270 microprocessor, or on an Advanced Digital Logic PC104 [39] running Fedora Linux for applications requiring greater computation power. A common program was written for both aircraft configurations that manages control and sensing in real-time.

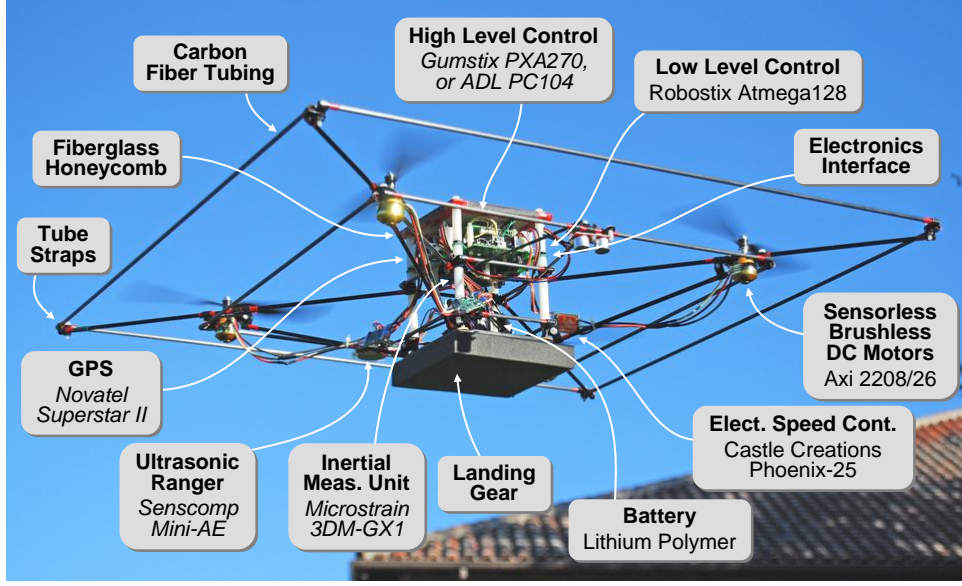


Figure 11: STARMAC II vehicle and its components.

4.2. Sensors

The sensor suite is comprised of two categories of sensors—those used to estimate the vehicle state and those used to perceive the surrounding environment. Measurements from the vehicle state sensors are used for attitude, position, and path tracking control algorithms, as will be described in Section 5. The sensors for the surrounding environment will be used for automated search and rescue, obstacle detection, and simultaneous localization and mapping.

The vehicle is equipped with three sensors for vehicle state estimation, all of which are fused using an Extended Kalman Filter (EKF). Measurements are fused from a Microstrain 3DM-GX1 inertial measurement unit (IMU), a downward facing Senscomp Mini-AE ultrasonic rangefinder, and integrated carrier phase (ICP) measurements from a Novatel Superstar II GPS receiver. For the GPS, a custom code was developed in house, providing 10 Hz position and velocity estimates with an accuracy of 0.02-0.05 m relative to a stationary base station. The code is executed in the background in real-time on existing on-board computers. For indoor flights, an overhead USB camera was used in conjunction with hue blob tracking software to provide position sensing in place of GPS for the flights presented in this paper. The camera system gives 0.01-0.02 m accuracy at 15 Hz, and combined with ultrasonic measurements of the range to the floor, provides a drop-in replacement for GPS input to the EKF. The camera system has been subsequently replaced with a VICON position-tracking system.

To perceive the surrounding environment, the vehicle frame can be reconfigured to carry additional sensors for specific applications. Numerous additional sensors have been tested on the STARMAC platform, including the Videre Systems stereo vision camera [40], various USB cameras, the Hokuyo URG-04LX laser range finder [41], and the Tracker DTS digital avalanche rescue beacon and receiver [42]. These sensors were selected to enable potential autonomous multi-agent missions, such as cooperative search and rescue [1].

5. Control System

A hierarchical approach to vehicle control was adopted for STARMAC II. This section gives the results of this controls development process in order from the inner attitude and altitude loops to the position and trajectory tracking loops. A feedforward compensator adjusts for the aerodynamic effects discussed in Section 3.

5.1. Attitude and Altitude Control

At small angles (roughly $\pm 30^\circ$), the equations of motion are approximately decoupled about each attitude axis, so control input moments about each axis, u_ϕ , u_θ , and u_ψ , can be implemented independently. The inputs for each axis

are added to the total thrust control input u_z to generate thrust commands u_1 through u_4 , for motors 1 through 4,

$$\begin{aligned} u_1 &= u_\theta/L + u_\psi/(4\kappa_t) + u_z/4 \\ u_2 &= -u_\phi/L - u_\psi/(4\kappa_t) + u_z/4 \\ u_3 &= -u_\theta/L + u_\psi/(4\kappa_t) + u_z/4 \\ u_4 &= u_\phi/L - u_\psi/(4\kappa_t) + u_z/4 \end{aligned} \quad (18)$$

where L is the distance between rotor centers and the \mathbf{z}_B axis. The time delay in thrust is well approximated as a first order delay with time constant τ , as experimentally verified [34], and found to be 0.1 s for STARMAC II. The resulting transfer function for the roll axis is

$$\frac{\Phi(s)}{U_\phi(s)} = \frac{1/I_\phi}{s^2(\tau s + 1)} \quad (19)$$

where I_ϕ is the component of I_B for the roll axis. The transfer functions for the pitch and yaw axes are analogous. Note that the induced power and blade flapping effects are not included in the linear model; they are compensated using feed forward compensation described in Section 5.2. Any inaccuracies in this model or complications such as vortex ring state are treated as disturbance forces and moments that must be rejected by the control system.

Although a standard proportional-integral-derivative (PID) controller has been shown to perform adequately [37], control design using root locus techniques revealed that an additional zero, giving angular acceleration feedback, allowed the gains to be significantly increased, yielding higher bandwidth. Further, acceleration compensation gives direct feedback on the actual thrust achieved, regardless of vortex ring state or ascent/descent dynamics of Section 3-3.2. The resulting control law,

$$C(s) = k_{dd}s^2 + k_d s + k_p + \frac{k_i}{s} \quad (20)$$

was tuned to provide substantially faster and more accurate performance than previously possible for maneuvering vehicles (see Figures 12 and 13). The time-domain control input for the roll axis is then

$$u_\phi = k_{dd}(\ddot{\phi}_{ref} - \ddot{\phi}) + k_d(\dot{\phi}_{ref} - \dot{\phi}) + k_p(\phi_{ref} - \phi) + k_i \int_0^t (\phi_{ref} - \phi) dt \quad (21)$$

with the time-domain angular control inputs u_θ and u_ψ generated similarly. Anti-windup is used for the integral term.

Angular accelerations must be computed by finite differencing the rate gyroscope data, a step that can amplify noise. However, in implementation, the values computed from differencing of angular velocity measurements at 76 Hz had sufficiently low noise for use in the controller.

In practice, the controller is able to track rapidly varying reference commands, as shown in Figure 13, with root mean square (RMS) error of 0.65° in each axis. Aggressive flights have been flown frequently, with typically up to 15° of bank angle. The controller has been flown up to its programmed limit of 30° without significant degradation in performance.

A similar approach using linear acceleration was taken for altitude control and found to greatly improve performance. Feedback linearization is used to compensate for the offset of gravity and the deflection of thrust due to tilt,

$$u_z = \frac{1}{\cos \phi \cos \theta} (k_{dd,alt}(\ddot{z}_{ref} - \ddot{z}) + k_{d,alt}(\dot{z}_{ref} - \dot{z}) + k_{p,alt}(z_{ref} - z)) + T_{nom} \quad (22)$$

where z is the altitude and z_{ref} is the reference command. The linearized plant model is identical in form to Eq. (19). Results for the altitude control loop are presented in Figure 14.

5.2. Feedforward Compensation for Aerodynamic Effects

Although the control scheme detailed above is quite successful at rejecting small disturbances, it is unable to reject the large systematic disturbances that result from the aerodynamic effects described in Section 3. A feedforward compensation scheme is thus used to calculate and cancel out moments and forces resulting from blade flapping and variations in total thrust. Feedback through the control loops helps protect against model uncertainty.

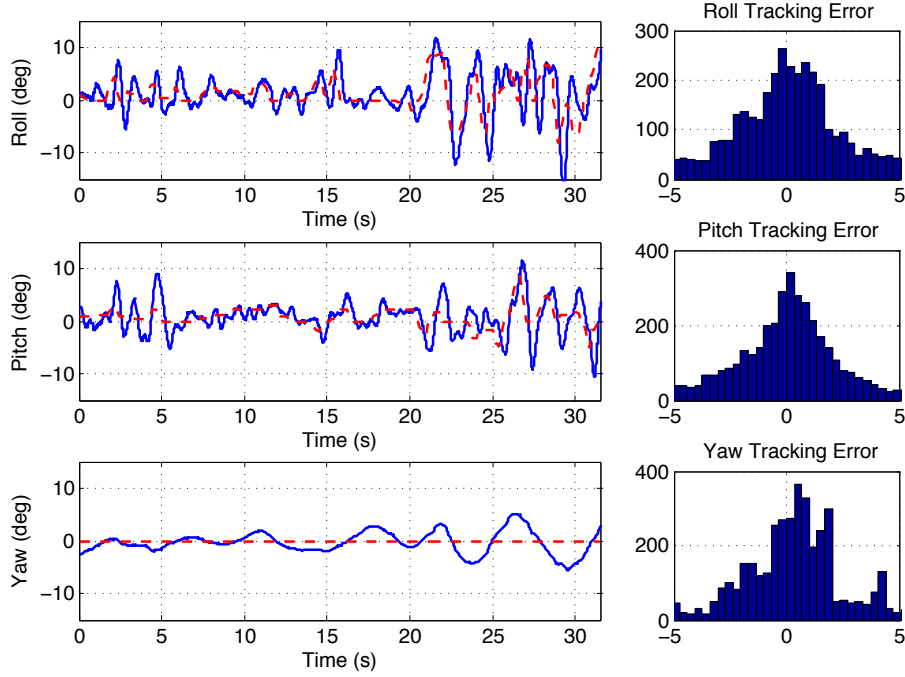


Figure 12: Attitude control results from indoor flight tests for roll, pitch and yaw without angular acceleration damping. Histograms of tracking error (in degrees) are on the right.

5.2.1. Calculation of Forces and Moments

Compensation for blade flapping is accomplished by estimating the moment on the vehicle due to the deflection of the thrust vector, and then commanding an equivalent but opposing moment. The flap angle is well approximated as being linearly proportional to velocity, and at the angles currently flown (up to 30°) the effects can be decomposed in the body axes. Thus the flap angle along the body x axis $a_{1s,x}$ is

$$a_{1s,x} = k_f v_{b,x} \quad (23)$$

where $v_{b,x}$ is the velocity in the body x axis and k_f is an experimentally derived constant relating flap angle to velocity. The corresponding pitch moment M_θ needed to compensate is then

$$M_\theta = -4(k_\beta a_{1s,x} + Th \sin a_{1s,x}) \approx -4(k_\beta + Th)a_{1s,x} \quad (24)$$

and a similar compensating moment is calculated for the roll axis.

Thrust compensation is achieved by calculating a nominal thrust T_h that is needed to generate an actual, desired thrust T and then sending this T_h command to the motors. From Equation (7), the ratio of commanded hover thrust T_h to actual thrust for a given power is

$$\frac{T_h}{T} = \frac{v_h}{v_i - v_\infty \sin \alpha} \quad (25)$$

The desired thrust T is calculated by the attitude and altitude controllers, and T_h is a function of v_h . Solving Equations (6) and (25) for v_h and v_i then allow the hover thrust T_h to be calculated from v_h . However, since the resulting equations are quartic in the unknown variables, a lookup table is used for computational efficiency.

5.2.2. Compensation Flight Results

To demonstrate the effect of the aerodynamic control compensation, a STARMAC quadrotor was flown on a series of test flights that consisted of forward flight with a large attitude command in one direction, followed by a sudden

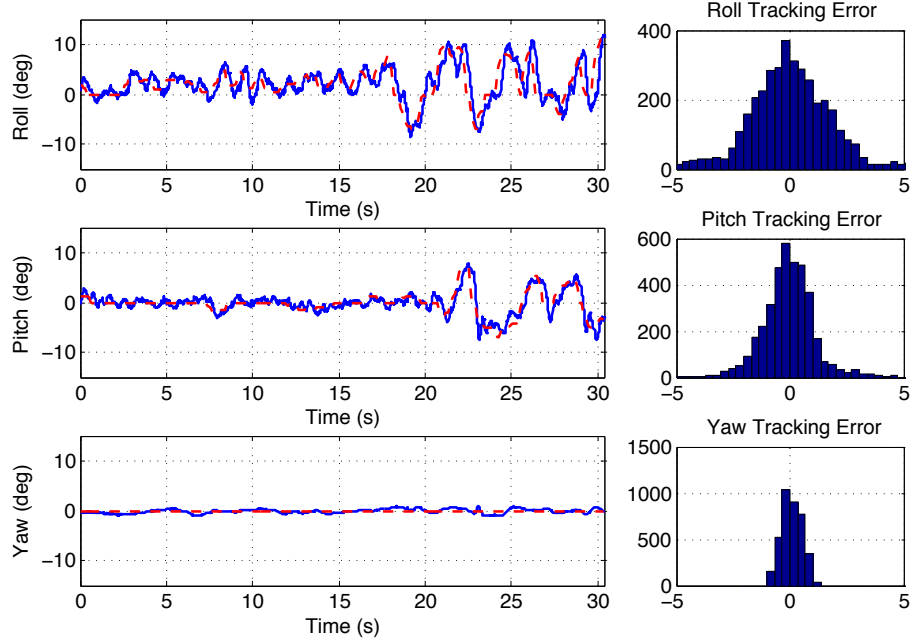


Figure 13: Attitude control results from indoor flight tests with angular acceleration damping. Histograms of tracking error on the right. Performance is much improved over Figure 12.

reversal in attitude and direction. Results for blade flapping are presented in Figure 15, and for thrust variation in Figure 16.

Attitude tracking results are shown in Figure 15. Both simulated and actual flight results are shown, with the flight results showing data averaged over 6 flights each for compensated and uncompensated controllers. The results demonstrate good tracking performance with compensation for flapping, with the uncompensated controller showing sustained tracking errors of up to 5° . The results match well with the simulation, validating the flight models used. Note that the simulation results also show results from a controller using large integral gain for attitude tracking. Although this controller is able to compensate for the flapping moment, it results in large overshoots. Flight results are not demonstrated for this controller since test flights with high integral gain resulted in large overshoots and near instability under nominal flight conditions.

Altitude tracking results for both simulation and a representative flight test are shown in Figure 16. The sudden change in angle of attack from the maneuver causes an large increase in thrust, which if not compensated for causes a large climb that the altitude controller must then settle out. By compensating for the increase in thrust, the vehicle is able to avoid this large transient error. However, there is an unexplained transient behavior that causes the vehicle to drop in altitude at the end of the flight, as seen in Figure 16(b). The authors were unable to reproduce this sudden descent in simulation using the models described in Section 3, and it is currently unclear what may be causing the effect.

5.3. Position and Trajectory Tracking Control

Position control is accomplished using successive loop closure with the position control loop generating reference commands for the attitude control loop. Consider control in the \mathbf{e}_E direction. Using Eqs. (4) and (1) and a small angle approximation for $\sin \phi \approx \phi$, when $\psi = 0$, the transfer function is $\frac{X_E(s)}{\Phi(s)} = (T_{nom}/m)\frac{1}{s^2}$. Note that this neglects drag, induced power, and blade flapping. For this control design, those effects are again treated as disturbance forces that must be rejected by the control system. Setting the control input to $u_E = \phi_{ref}$, the open loop plant is the convolution

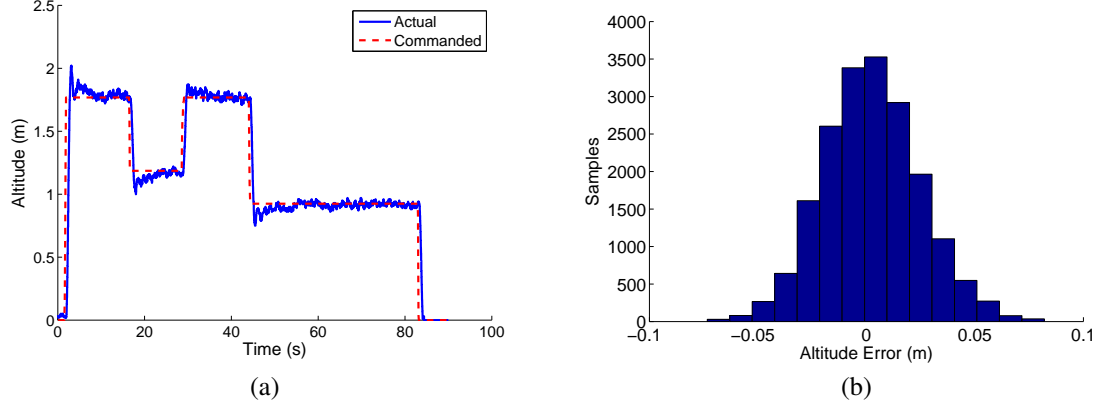


Figure 14: (a) Altitude command tracking in indoor flight tests. (b) Histogram of altitude error for 3 minute hover flight.

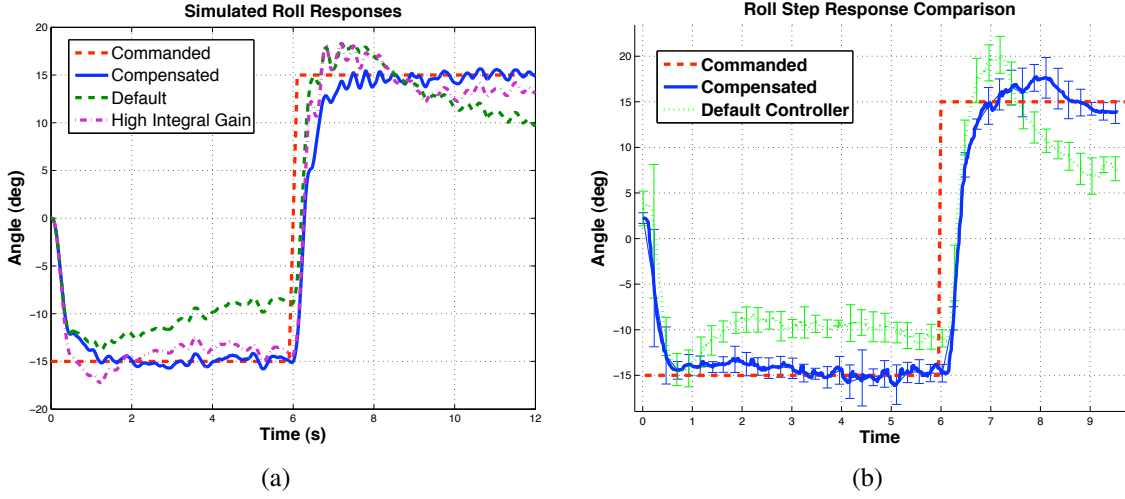


Figure 15: Comparison of attitude control with and without compensating for flapping. (a) Simulated results for large steps in roll. (b) Actual flight results from a series of 5 flights with each controller.

of the x_E dynamics with the closed loop dynamics of ϕ , Eq. (19), using the feedback control law of Eq. (20),

$$\frac{X_E(s)}{U_E(s)} = \frac{C(s)T_{nom}I_\phi/m}{s^2(\tau s^3 + s^2 + C(s)I_\phi)} \quad (26)$$

The open loop plant for the \mathbf{e}_N direction is analogous, using θ rather than ϕ . When $\psi \neq 0$, the control inputs must be rotated accordingly.

A PID controller was implemented using Eq. (26). The results for indoor flight tests are presented in Figure 17. The resulting RMS east and north error was 0.036 m. Using $C(s)$ rather than previous PID implementations for attitude control yielded superior closed loop position control.

Extending the position controller to track trajectories was accomplished by changing the relevant errors signals to along-track and cross-track error. A path, $\Lambda \in N \times \mathbb{R}^3$, is defined by a sequence of N desired waypoints, \mathbf{x}_k^d and desired speeds of travel v_k^d along path segment Λ_k connecting waypoint k to $k + 1$, as depicted in Figure 18. Let \mathbf{t}_k be the unit tangent vector in the direction of travel along the track from \mathbf{x}_k^d to \mathbf{x}_{k+1}^d , and \mathbf{n}_k be the unit normal vector to the

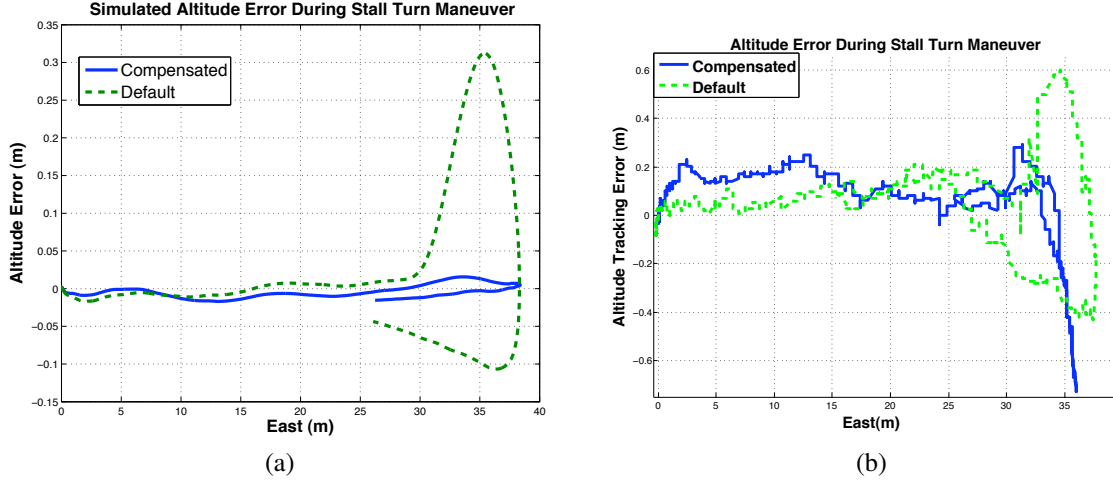


Figure 16: Comparison of altitude control with and without compensation for change in thrust due to sudden change in angle of attack, (a) in simulated flight (b) in actual flight.

track. Then, given the current position $\mathbf{x}(t)$, the cross-track error e_{ct} , error rate \dot{e}_{ct} and along-track error rate \dot{e}_{at} are,

$$\begin{aligned} e_{ct} &= (\mathbf{x}_k^d - \mathbf{x}(t)) \cdot \mathbf{n}_k \\ \dot{e}_{ct} &= -\mathbf{v}(t) \cdot \mathbf{n}_k \\ \dot{e}_{at} &= v_k^d - \mathbf{v}(t) \cdot \mathbf{t}_k \end{aligned} \quad (27)$$

Note that only the along-track error rate is considered, and depends only on the velocity of the vehicle. This is done so that the resulting controller does not attempt to catch up or slow down for scheduled waypoints, but simply proceeds along the track matching the desired velocity as closely as possible. This design choice assumes that the desired speed is selected, and the time of achieving a waypoint is unimportant. It is straightforward to extend the following control law by including feedback on along-track position, if timing is important.

The trajectory tracking controller was implemented by closing the loop on along-track rate error and cross-track error. This is essentially piecewise PI control in velocity in the along-track direction, and PID control in the cross-track direction,

$$\begin{aligned} u_{at} &= K_{d,at}\dot{e}_{at} + K_{i,at} \int_0^t \dot{e}_{at} dt \\ u_{ct} &= K_{p,ct}e_{ct} + K_{d,ct}\dot{e}_{ct} + K_{i,ct} \int_0^t \dot{e}_{ct} dt \end{aligned} \quad (28)$$

where control inputs u_{at} and u_{ct} are the attitude commands for vehicle tilt in the along-track and cross-track directions, respectively. They are rotated by ψ and by the trajectory orientation to generate ϕ_{ref} and θ_{ref} commands for the inner loop. Transition from segment k to $k+1$ occurs when the vehicle crosses the line segment normal to the path at the end of the segment. Upon completion of Λ_i , the integrators are reset. The trajectory controller presented here is intended for use with a coarse set of waypoints, focusing on accurate line tracking. It has been improved upon for finer resolution paths by computing feed forward inputs to follow a least-norm control input solution through the waypoints, though the details are out of the scope of this paper.

The controller defined in Eq. (28) was implemented on the STARMAC platform in both indoor and outdoor settings, with results presented in Figure 19. The indoor results demonstrate tracking errors of under ± 0.1 m throughout the box shaped trajectory, and show the largest overshoot when switching from one track to the next, as the desired direction of travel suddenly switches by 90° . For the outdoor flight tests, the gains on the cross-track and along-track controllers were reduced significantly, and the resulting errors increased to ± 0.5 m. Lower gains were used due to increased oscillations when in hover condition outside, and may be attributed to either significant wind gust disturbances or to the decreased position update rate from 15 Hz for the indoor positioning system to 10 Hz for the carrier phase differential GPS solution.

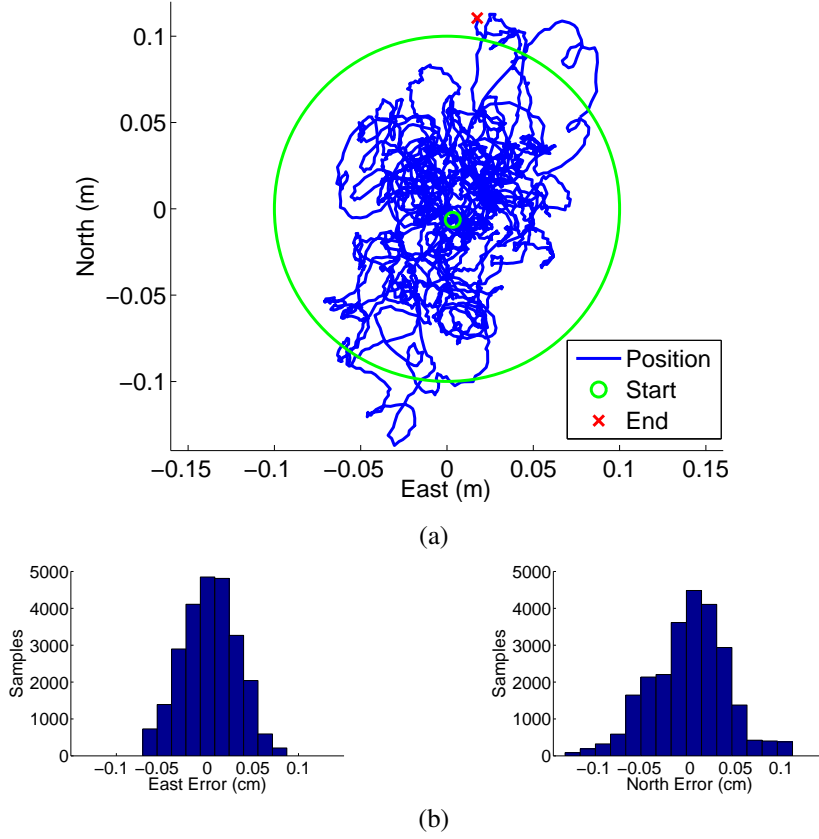


Figure 17: Autonomous indoor hover performance. (a) Position plot over 3 minutes of flight with 0.1 m error circle. (b) Histogram of position error in North and East directions.

This trajectory controller has some interesting properties. Since the path is composed only of line segments, overshoot on sharp corners is inevitable, a systematic tracking error. This is addressed by the alternative option using least-norm feed forward inputs, as described above. Another property arises due to the lack of mandated times to be at each waypoint. The trajectory tracking controller does not deviate from the intended path to try to meet a deadline—a required feature when the path is meant to avoid obstacles.

5.4. Applications

The precise, accurate control enabled by the controllers described above have allowed STARMAC to become a useful and flexible research platform. Although the details of these applications are outside the scope of this paper, a brief discussion of several flight experiments will be presented to highlight the utility of the STARMAC quadrotors in developing and demonstrating multi-vehicle control algorithms.

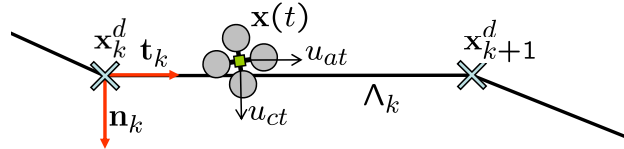


Figure 18: The quadrotor travels along path segment Λ_k from waypoint \mathbf{x}_k^d to \mathbf{x}_{k+1}^d , applying along and cross-track control inputs to track the path.

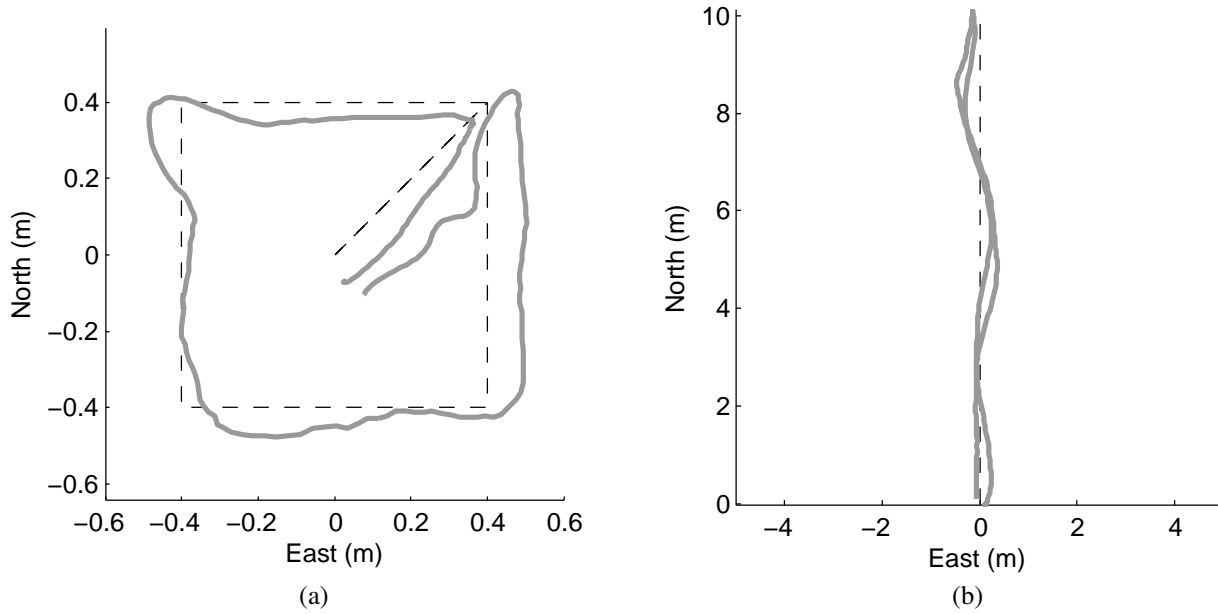


Figure 19: Tracking a trajectory (a) indoors, at 0.5 m/s, with an error of under 0.1 m, and (b) outdoors, at 2.0 m/s, with an error of under 0.5 m.

Decentralized multi-vehicle collision avoidance is a very important issue for multi-vehicle systems. STARMAC was used to demonstrate a decentralized algorithm designed to generate optimal, collision-free trajectories using Nash Bargaining [12]. For the flight test, three STARMAC quadrotors were placed such that their desired trajectories would result in violating a minimum separation distance. The quadrotors communicated with each other to generate safe trajectories using only their onboard computation, and successfully flew these trajectories (see Figure 20a).

Another important task for UAVs is performing obstacle avoidance in tight areas. For this particular experiment, a minimum-time, optimal trajectory was generated from an obstacle map using the Tunnel-MILP algorithm [15, 16]. This trajectory was generated off-board and transmitted to a STARMAC quadrotor, which then successfully bypassed the obstacles placed in the field. Figure 20b shows both the obstacle field and the desired and actual trajectories of the STARMAC quadrotor.

Finally, another experiment was conducted using a pair of STARMAC quadrotors to cooperatively locate a magnetic avalanche rescue beacon [43]. The STARMAC quadrotors used onboard avalanche rescue sensors to update particle filter representations of the location of an unknown beacon (blue dots in Figure 20c) and used an information-theoretic approach to generate trajectories that maximized information gain [13, 14]. All optimization and control was performed using the on-board PC104 computers.

6. Conclusion

This work describes in detail the vehicle dynamics, vehicle design, and control system design of the STARMAC quadrotor testbed. With the successful completion of autonomous trajectory tracking flight demonstrations on the quadrotor helicopters of the STARMAC platform, a major milestone has been achieved not only for the testbed but also for the development of quadrotors as viable autonomous micro-aerial vehicles. The many lessons learned in the process of developing these vehicles should be of significant utility to any other groups interested in accessible, trouble-free UAV development.

Many exciting avenues of future investigations are now possible. For example, the incorporation of the aerodynamic effects outlined in Section 3 into the trajectory tracking control law will allow for more precise tracking and therefore enable high speed operation in cluttered environments. Similarly, the expansion of multi-vehicle capabilities is now a priority, as is the incorporation of additional sensors to enable on-board estimation of and operation in

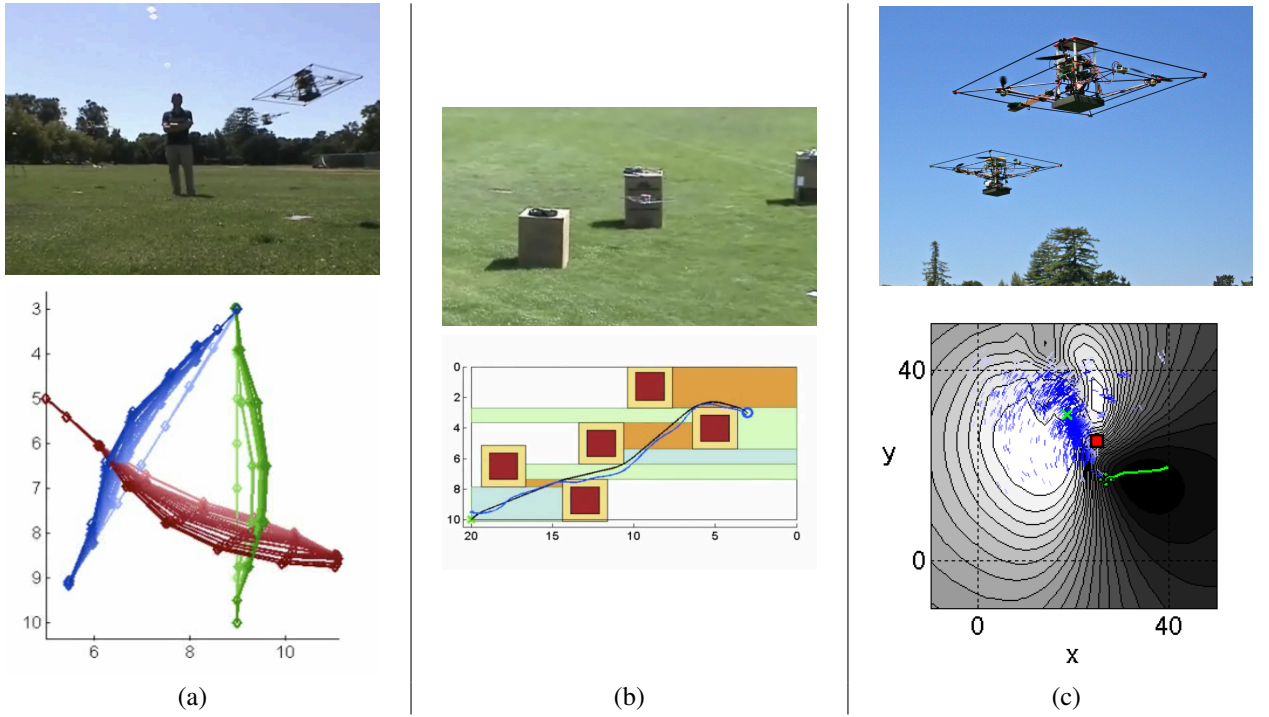


Figure 20: Experimental flight tests conducted using the STARMAC platform and controllers discussed in this paper showing (a) decentralized cooperative collision avoidance using Nash bargaining; flight experiment and iterative solutions, (b) obstacle avoidance using the Tunnel-MILP algorithm; flight experiment and computed path through the tunnel decomposition, and (c) information-theoretic cooperative search; quadrotors carrying beacon receivers and mutual information contours for one vehicle

unknown environments. With STARMAC, a reliable, capable and convenient testbed of autonomous aerial vehicles, the multi-vehicle applications for which it was developed are now clearly within reach.

Acknowledgments

The authors would like to thank Jung Soon Jang, David Shoemaker, David Dostal, Dev Gorur Rajnarayan, Vijay Pradeep, Paul Yu, Justin Hendrickson, and Michael Vitus, for their many contributions to the development of the STARMAC testbed. We would also like to thank Mark Woodward for the image processing program used for the USB camera system.

References

- [1] G. M. Hoffmann, S. L. Waslander, C. J. Tomlin, Distributed cooperative search using information-theoretic costs for particle filters with quadrotor applications, in: Proc. AIAA Guidance, Navigation, and Control Conf., Keystone, CO.
- [2] Liz Hull, Drone makes first UK 'arrest' as police catch car thief hiding under bushes, Daily Mail Online, 2010. <http://www.dailymail.co.uk/news/article-1250177/Police-make-arrest-using-unmanned-drone.html>.
- [3] Microdrones GmbH, MD4-200 quadrotor helicopter, 2008. http://www.microdrones.com/news_waypoint_navigation.html.
- [4] Ascending Technologies GmbH, AscTec hummingbird, 2008. <http://www.asctec.de>.
- [5] DraganFly-Innovations, DraganFlyer X4 (2009). <http://www.rctoys.com>.
- [6] Aeryon Labs Inc., Aeryon Scout (2009). www.aeryon.com.
- [7] M. Valenti, B. Bethke, G. Fiore, J. P. How, E. Feron, Indoor multi-vehicle flight testbed for fault detection, isolation, and recovery, in: Proc. AIAA Guidance, Navigation, and Control Conf., Keystone, CO.
- [8] M. Achtelik, A. Bachrach, R. He, S. Prentice, N. Roy, Autonomous navigation and exploration of a quadrotor helicopter in GPS-denied indoor environments, in: AUVSI First Symposium on Indoor Flight Issues, Mayagüez, Puerto Rico.
- [9] N. Michael, J. Fink, V. Kumar, Cooperative manipulation and transportation with aerial robots, Robotics: Science and Systems, (Seattle, WA) (2009).
- [10] S. Lupashin, A. Schöllig, M. Sherback, R. DAndrea, A simple learning strategy for high-speed quadcopter multi-flips (2010).
- [11] S. L. Waslander, G. Inalhan, C. J. Tomlin, Decentralized optimization via nash bargaining, in: D. Grunzel, R. Murphey, P. M. Pardalos (Eds.), Theory and Algorithms for Cooperative Systems, volume 4, World Scientific Publishing Co., 2004, pp. 565–585.
- [12] S. L. Waslander, C. J. Tomlin, Decentralized optimization and the nash bargaining solution for autonomous collision avoidance, submitted to IEEE Transactions on Control Systems Technology (2010).
- [13] G. M. Hoffmann, S. L. Waslander, C. J. Tomlin, Mutual information methods with particle filters for mobile sensor network control, in: Proc. 45th IEEE Conf. Decision and Control, San Diego, CA, pp. 1019–1024.
- [14] G. M. Hoffmann, C. J. Tomlin, Mobile sensor network control using mutual information methods and particle filters, IEEE Transactions on Automatic Control 55 (2010) 32–47.
- [15] M. Vitus, V. Pradeep, G. M. Hoffmann, S. L. Waslander, C. J. Tomlin, Tunnel-MILP: Path planning with sequential convex polytopes, in: 2008 AIAA Guidance, Navigation and Control Conference and Exhibit, Honolulu, Hawaii, USA.
- [16] M. P. Vitus, S. L. Waslander, C. J. Tomlin, submitted to the IEEE Journal of Robotics (2010).
- [17] J. Gillula, H. Huang, M. P. Vitus, C. J. Tomlin, Design of guaranteed safe maneuvers using reachable sets: Autonomous quadrotor aerobatics in theory and practice, in: In the Proceedings of the 2010 IEEE International Conference on Robotics and Automation, Anchorage, Alaska.
- [18] S. Newman, The Foundations of Helicopter Flight, Halsted Press, New York, NY, pp. 107–116.
- [19] J. G. Leishman, Principles of Helicopter Aerodynamics, Cambridge University Press, New York, NY, pp. 36–71.
- [20] R. W. Prouty, Helicopter Performance, Stability, and Control, Krieger Publishing Company, Malabar, FL, pp. 143–146, 476–477.
- [21] E. Altuğ, J. P. Ostrowski, C. J. Taylor, Quadrotor control using dual camera visual feedback, in: Proc. IEEE Int. Conf. on Robotics and Automation, Taipei, Taiwan, pp. 4294–4299.
- [22] DraganFly-Innovations, DraganFlyer V (2008). <http://www.rctoys.com>.
- [23] S. Bouabdallah, P. Murrieri, R. Siegwart, Towards autonomous indoor micro vtol, Autonomous Robots 18 (2005) 171–183.
- [24] P. Pounds, R. Mahony, J. Gresham, P. Corke, J. Roberts, Towards dynamically-favourable quad-rotor aerial robots, in: Proc. of the Australasian Conf. on Robotics and Automation, Canberra, Australia.
- [25] P. Pounds, R. Mahony, P. Corke, Modelling and control of a quad-rotor robot, in: Proc. of the Australasian Conf. on Robotics and Automation, Auckland, New Zealand.
- [26] P. Pounds, R. Mahony, P. Corke, Modelling and control of a large quadrotor robot, Control Engineering Practice 18 (2010) 691–699.
- [27] G. Hoffmann, D. G. Rajnarayan, S. L. Waslander, D. Dostal, J. S. Jang, C. J. Tomlin, The stanford testbed of autonomous rotorcraft for multi agent control (starmac), in: Proc. 23rd Digital Avionics Systems Conf., Salt Lake City, UT, pp. 12.E.4/1–10.
- [28] N. Guenard, T. Hamel, V. Moreau, Dynamic modeling and intuitive control strategy for an x4-flyer, in: Proc. IEEE Int. Conf. on Robotics and Automation, Budapest, Hungary, pp. 141–146.
- [29] J. Escareño, S. Salazar-Cruz, R. Lozano, Embedded control of a four-rotor uav, in: Proc. AACC Amer. Control Conf., Minneapolis, MN, pp. 3936–3941.
- [30] E. B. Nice, Design of a Four Rotor Hovering Vehicle, Master's thesis, Cornell University, 2004.
- [31] S. Park, et al., Ric (robust internal-loop compensator) based flight control of a quad-rotor type uav, in: IEEE/RSJ Int. Conf. on Intelligent Robotics and Syst., Edmonton, Alberta.

- [32] S. Craciunas, C. Kirsch, H. Röck, R. Trummer, The javiator: A high-payload quadrotor uav with high-level programming capabilities, Proc. GNC. AIAA (2008).
- [33] J. Courbon, Y. Mezouar, N. Guénard, P. Martinet, Vision-based navigation of unmanned aerial vehicles, Control Engineering Practice 18 (2010) 789–799.
- [34] G. M. Hoffmann, H. Huang, S. L. Waslander, C. J. Tomlin, Quadrotor helicopter flight dynamics and control: Theory and experiment, in: Proc. AIAA Guidance, Navigation, and Control Conf., Hilton Head, SC.
- [35] H. Huang, G. M. Hoffmann, S. L. Waslander, C. Tomlin, Aerodynamics and control of autonomous quadrotor helicopters in aggressive maneuvering, in: Proc. IEEE Int. Conf. on Robotics and Automation, Kobe, Japan, pp. 3277–3282.
- [36] W. Johnson, Helicopter Theory, Princeton University Press, Princeton, NJ, pp. 126–131.
- [37] S. L. Waslander, G. M. Hoffmann, J. S. Jang, C. J. Tomlin, Multi-agent quadrotor testbed control design: Integral sliding mode vs. reinforcement learning, in: IEEE/RSJ Int. Conf. on Intelligent Robotics and Syst., Edmonton, Alberta, pp. 468–473.
- [38] G. E. Computers, Robostix and Verdex Boards, 2008. <http://www.gumstix.com/>.
- [39] Advanced Digital Logic, ADL855 PC104+, 2008. <http://www.adlogic-pc104.com/products/cpu/pc104/datasheets/MSM855.pdf>.
- [40] Videre Design, STH-MDCS 2 Stereo Vision Head, 2008. <http://www.videredesign.com/sthmdcs2.htm>.
- [41] Hokuyo, URG-04LX Laser Range Finder, 2008. <http://www.hokuyo-aut.jp/products/urg/urg.htm>.
- [42] BackCountry Access, Tracker DTS Digital Avalanche Beacon, 2008. http://www.bcaccess.com/bca_products/tracker/index.php.
- [43] G. M. Hoffmann, Autonomy for Sensor-Rich Vehicles: Interaction between Sensing and Control Actions, Ph.D. thesis, Stanford University, 2008.